

# Single-molecule mid-infrared spectroscopy and detection through vibrationally assisted luminescence

Received: 28 October 2022

Accepted: 2 July 2023

Published online: 28 August 2023

 Check for updates

Rohit Chikkaraddy<sup>1,2</sup>✉, Rakesh Arul<sup>1</sup>, Lukas A. Jakob<sup>1</sup>  
& Jeremy J. Baumberg<sup>1</sup>✉

Room-temperature detection of molecular vibrations in the mid-infrared (MIR,  $\lambda = 3\text{--}30\ \mu\text{m}$ ) has numerous applications, including real-time gas sensing, medical imaging and quantum communication. However, existing technologies rely on cooled semiconductor detectors because of thermal noise limitations. One way to overcome this challenge is to upconvert the low-energy MIR photons into high-energy visible wavelengths ( $\lambda = 500\text{--}800\ \text{nm}$ ) where detection of single photons is easily achieved using silicon technologies. This process suffers from weak cross-sections and the MIR-to-visible wavelength mismatch, limiting its efficiency. Here we exploit molecular emitters possessing both MIR and visible transitions from molecular vibrations and electronic states, coupled through Franck-Condon factors. By assembling molecules into a plasmonic nanocavity resonant at both MIR and visible wavelengths, and optically pumping them below the electronic absorption band, we show transduction of MIR light. The upconverted signal is observed as enhanced visible luminescence. Combining Purcell-enhanced visible luminescence with enhanced rates of vibrational pumping gives transduction efficiencies of  $>10\%$ . MIR frequency-dependent upconversion gives the vibrational signatures of molecules assembled in the nanocavity. Transient picocavity formation further confines MIR light down to the single-molecule level. This allows us to demonstrate single-molecule MIR detection and spectroscopy that is inaccessible to any previous detector.

Atomic bonds possess mid-infrared (MIR) resonances corresponding to vibrational transitions. Although these are thermally populated at room temperature, electronic states with transition energies in the visible have negligible thermal occupation. While detection of visible light is efficient down to the single-photon level<sup>1,2</sup>, the detection of MIR photons remains challenging<sup>3-7</sup>; however, these states can be engineered to interact. Quantum systems in which vibrations are coupled to electronic transitions have already proven fertile for

quantum manipulation, for instance by using trapped ions that are entangled through their vibrational motions in a trap<sup>8</sup>. More recent efforts to create solid-state quantum platforms have exploited quantum dots or defect centres embedded in micro-mechanical resonators as optomechanical transducers<sup>9,10</sup>. In this article, we demonstrate their ultimate scaling-down to the sub-nanometre scale, by coupling electronic and vibrational transitions in molecular bonds, down to single emitter molecules. This provides a way to perform MIR spectroscopy of

<sup>1</sup>NanoPhotonics Centre, Cavendish Laboratory, Department of Physics, University of Cambridge, Cambridge, UK. <sup>2</sup>School of Physics and Astronomy, University of Birmingham, Birmingham, UK. ✉e-mail: [r.chikkaraddy@bham.ac.uk](mailto:r.chikkaraddy@bham.ac.uk); [jjb12@cam.ac.uk](mailto:jjb12@cam.ac.uk)

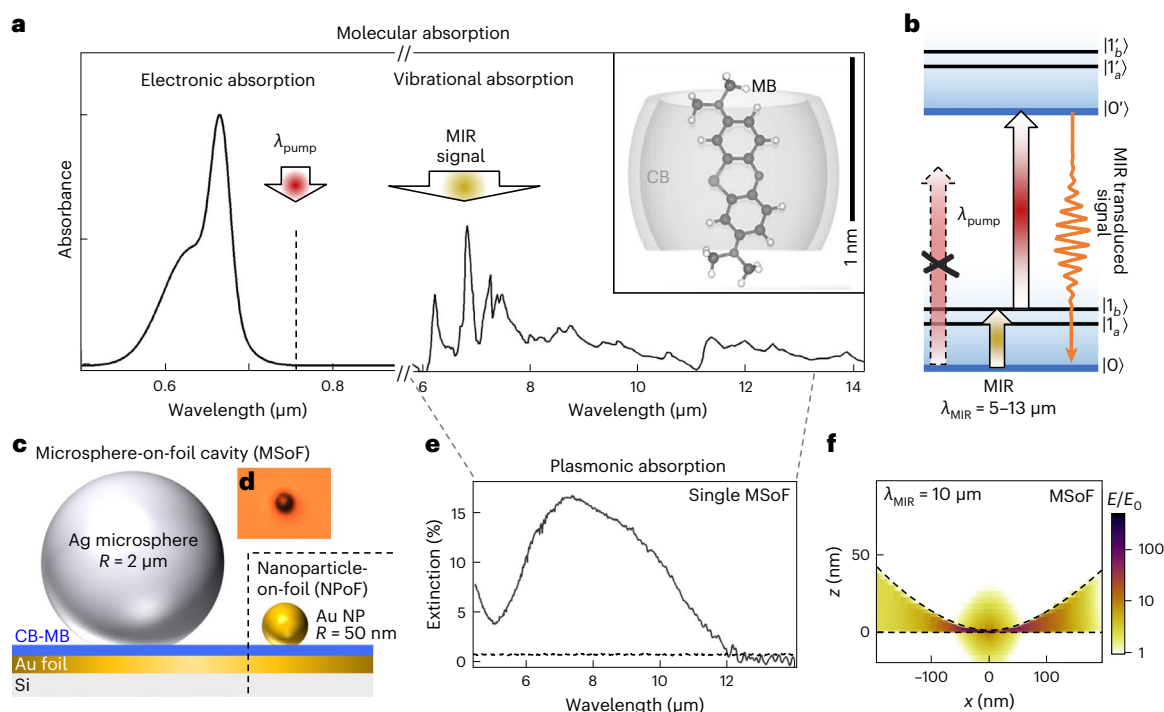


**Fig. 1 | MIR vibrationally assisted luminescence.** **a**, Electronic and vibrational absorption spectra of an MB molecule in solution. Arrows indicate NIR and MIR tuning. Inset: supramolecular assembly of MB inside a cucurbit[7]uril (CB) host molecule. **b**, Energy diagram of the electronic and vibrational levels of the MB molecule, indicating that the NIR pump (red arrow) drives the electronic transition only in the presence of MIR (yellow arrow). **c**, Silver-coated

microsphere constructed on a thin metal foil (MSof) as well as the alternative gold nanoparticle-on-foil (NPof) construct. **d**, Bright-field optical image of an individual MSof construct. **e**, Fourier-transform infrared spectroscopy of an individual MSof cavity assembled with a monolayer of MB-CB (solid grey line), compared to simulated extinction of the NPoF cavity (dotted grey line). **f**, Simulated near field of the MSof cavity at  $\lambda_{\text{MIR}} = 10 \mu\text{m}$ .

individual molecules via the detection of MIR light, which is normally hindered by thermal noise<sup>11</sup>, by upconverting the low-energy photons to visible wavelengths.

The need for ultrasensitive upconversion to perform single-molecule vibrational spectroscopy is further motivated by the desire to gain a deeper understanding of the molecular-scale processes underlying chemical and biological systems<sup>12</sup>. Although fluorescence spectroscopy and surface-enhanced Raman spectroscopy<sup>13,14</sup> have provided valuable insights into chemical catalysis, what is missing is the ability to study infrared-active (but Raman-inactive) molecular vibrations at the single-molecule level. Upconversion methods can potentially fill this gap and provide an improved understanding of complex systems and materials.

Demonstrations of MIR upconversion detection predominantly use parametric mixing in nonlinear crystals<sup>6</sup>, interferometric upconversion with entangled photon pairs<sup>15</sup> or non-degenerate two-photon absorption<sup>16</sup>. These methods require high-intensity ultrafast pulsed lasers to drive the nonlinear susceptibilities. In optomechanical cavity-assisted wave-mixing, MIR detection is possible through specific vibrational bonds that are both infrared and Raman active<sup>17,18</sup>, but the Raman cross-sections are intrinsically low.

Here we show MIR vibrationally assisted luminescence (MIRVAL) from molecular emitters. This scheme exploits the coupling between visible electronic transitions and the MIR vibrational transitions in a molecule. The electronic and vibrational absorption spectra of methylene blue (MB) molecules (Fig. 1a) show a strong dipolar electronic transition of MB at 665 nm corresponding to ground state to first singlet excited-state absorption ( $|0\rangle \rightarrow |0'\rangle$ )<sup>19</sup>. The vibronically mediated absorption  $|0\rangle \rightarrow |1'\rangle$  appears as a shoulder peak at 620 nm. When MB absorbs wavelengths shorter than 700 nm, the electronically excited molecule relaxes to the ground state via down-shifted

photoluminescence emission at 680 nm ( $|0'\rangle \rightarrow |0\rangle$ ) and 710 nm ( $|0'\rangle \rightarrow |1\rangle$ )<sup>20</sup>.

In our MIR detection scheme, the molecule is primed with continuous-wave (c.w.) pumping ( $\lambda_{\text{pump}} \geq 750 \text{ nm}$ ) at energies below the MB absorption band, so no photoluminescence is observed (Fig. 1b). In the presence of MIR light, specific vibrational levels in each molecule become populated ( $|0\rangle \rightarrow |1'_a\rangle, |1'_b\rangle$ ) in the ground electronic state. Here,  $|1'_a\rangle, |1'_b\rangle$  are different bond vibrations  $a, b$  within the MB molecule. Once the vibrational states are populated, the absorption of the pump becomes energetically allowed and drives the molecule from the ground state to the electronically excited state ( $|1'_a\rangle, |1'_b\rangle \rightarrow |0''\rangle$ ). This transition now relaxes to the ground state, giving photoluminescence at wavelengths shorter than the pump, resulting in anti-Stokes photoluminescence (aS-PL) and forming the MIR transduced signal. Such vibrationally assisted photoluminescence is analogous to the optical spin readout methods recently developed to record the NMR of quantum systems at the nanoscale<sup>21,22</sup>.

At room temperature, vibrational decays ( $10^{-12} \text{ s}$ ) are 1,000-fold faster than electronic decays ( $10^{-9} \text{ s}$ ), limiting the normal transduction efficiency of isolated molecules to  $<10^{-7}$  for c.w. pumping<sup>7</sup>. Although aS-PL can be observed for intense pulsed excitation<sup>23,24</sup>, such requirements are not practical for compact MIR detectors. To overcome this, here the molecules are placed inside a deep-subwavelength optical cavity formed of nanogap-spaced metallic surfaces, which can provide up to million-fold upconversion enhancements. The rate of light emission is Purcell-enhanced ( $P \propto 1/V$ , where  $V$  is the cavity mode volume), and the rate of excitation is also amplified by the optical near-field intensity ( $E^2$ ) at the location of the molecule, for a field  $E$  oriented along the molecular exciton's transition dipole. An ideal optical cavity will thus have the smallest mode volume with strong spatially overlapping near-field intensities at both pump and MIR wavelengths.

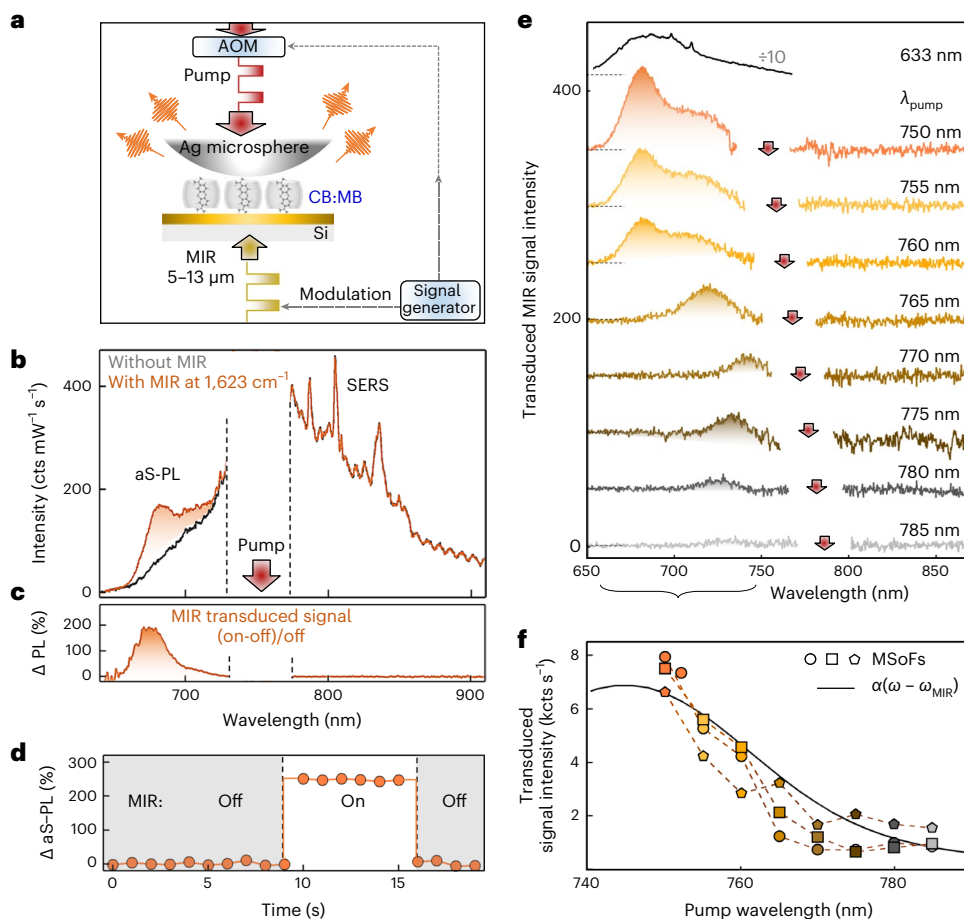


**Fig. 2 | Transduced MIR in vibrationally assisted luminescence.** **a**, MIR detection set-up with the pump illuminating an individual MSoF cavity. Incident light is modulated (dashed lines) by an acousto-optic modulator for the pump and a QCL laser for the MIR. **b**, Stokes and anti-Stokes emission from the pump, with (orange) and without (grey) MIR light of average power  $0.5 \mu\text{W} \mu\text{m}^{-2}$ , averaged over ten scans on a single MSoF cavity. **c**, Percentage difference in emitted signals transduced by MIR in **b**, PL, photoluminescence. **d**, Modulation of

aS-PL intensity switching the MIR beam on and off. **e**, MIR transduced signal when tuning the pump from  $\lambda_{\text{pump}} = 750 \text{ nm}$  (top) to  $785 \text{ nm}$  (bottom) in 5-nm steps (arrows indicate  $\lambda_{\text{pump}}$ ). Direct visible pumping at  $633 \text{ nm}$  is shown for comparison (top, grey curve). **f**, Spectrally integrated transduced signal from **e** versus  $\lambda_{\text{pump}}$  for three different MSoF cavities, compared with absorption spectra of MB molecules in solution, rigidly shifted by  $\omega_{\text{MIR}}$  (solid line).

To construct such small nanocavities with dual resonances tuned to the visible and MIR and containing molecules precisely oriented along the optical field, we used bottom-up nanoassembly. Silver-coated glass microspheres (AgMSs) were drop-cast onto a thin (10 nm) foil of flat Au with molecular emitters sandwiched in the gap formed between them (Fig. 1c). The resulting microsphere-on-foil (MSoF) device has a gap that can be accurately controlled (sub-nanometre), is straightforward to characterize, can be made easily and repeatably, and is scalable to large areas<sup>25,26</sup>. The diameter of each AgMS ( $2R = 4 \mu\text{m}$ ) was tuned to achieve MIR resonance with the intense plasmonic peak centred around  $8 \mu\text{m}$  (extinction coefficient of  $>10\%$ ; Fig. 1e). The interaction between each AgMS and its image in the underlying foil forms an effective dimer with strong electromagnetic enhancements ( $E^2/E_0^2 > 10^3$ ) perpendicular to the surface and an ultralow mode volume (Fig. 1f).

The molecular emitter MB was assembled into the nanogaps inside host macrocyclic cucurbit[7]uril (CB) molecules. CB provides a hydrophobic environment that isolates individual MB molecules and improves their photostability<sup>27</sup> (Fig. 1a). The carbonyl portals at either end of the 0.9-nm-high CB bind to Au, scaffolding the MB dipole near perpendicular to the metal surfaces for optimal coupling to the electromagnetic near field. We compared the MSoF with smaller-diameter nanoparticle-on-mirror (NPOF) constructs ( $2R = 0.1 \mu\text{m}$ ; Fig. 1c), which support a near-infrared (NIR) resonance, but only a broad non-resonant

MIR response (Fig. 1e, dotted grey line). Previous studies have shown that there are, on average,  $\bar{n} = 40$  MB molecules in the gap for 1% of CB filled with MB<sup>27</sup>. No photoluminescence was observed when the MSoF gaps were empty of MB dyes.

Assembling MSoF nanocavities on thin (200 μm) MIR-transparent silicon substrates allows MIR light to couple from the underside while simultaneously pumping from the top side (Fig. 2a) with visible laser irradiation. For improved signal-to-noise, both MIR and pump were modulated at 300 kHz. The emitted light from the MSoF construct was collected from the top side and routed to a monochromator-mounted silicon detector array after rejecting the pump beam with dielectric filters. The observed spectrum to lower (Stokes) energy shows surface-enhanced resonant Raman scattering (SERRS) peaks of the MB molecules assembled within the gap (Fig. 2b). In the absence of MIR light, anti-Stokes (higher energy) emission is attributed to electronic Raman scattering (ERS) from the metal<sup>28</sup>. In the presence of MIR light at  $1,623 \text{ cm}^{-1}$  the Stokes is unchanged, but on the anti-Stokes side we observe an upconverted photoluminescence peak at  $680 \text{ nm}$  corresponding to MB  $|0'\rangle \rightarrow |0\rangle$  emission. For  $\lambda_{\text{pump}} = 750 \text{ nm}$ , the effective wavelength of summed photon energies,  $1/\lambda = 1/\lambda_{\text{pump}} + 1/\lambda_{\text{MIR}} = 1/669 \text{ nm}$ , excites the  $|0\rangle \rightarrow |0'\rangle$  transition of MB. The MIR-transduced aS-PL intensity is increased by  $>180\%$  above the background (Fig. 2c) compared to without MIR light (Fig. 2d).

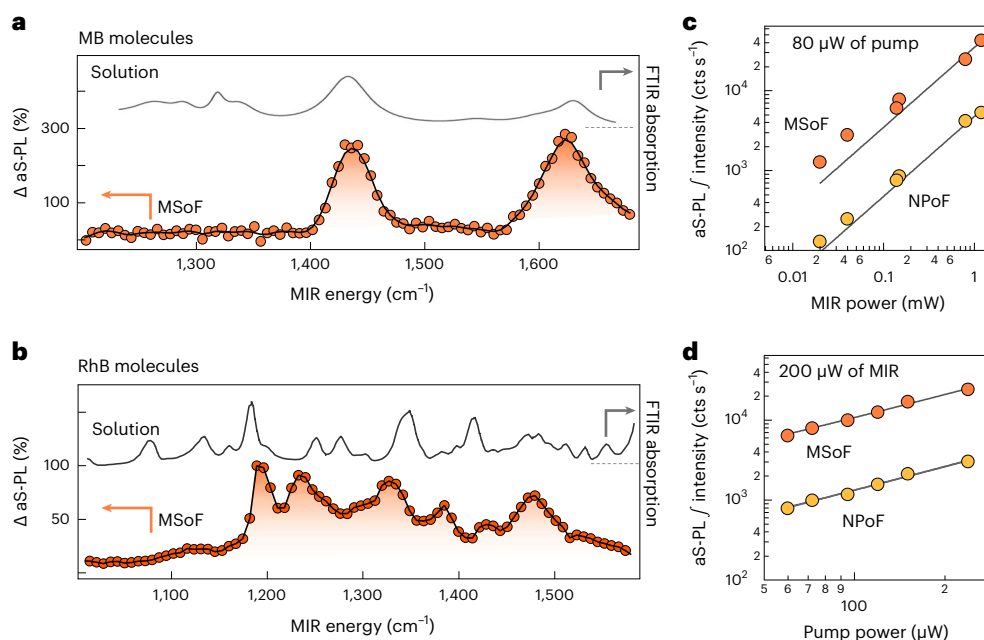


**Fig. 3 | MIR detection efficiency.** **a, b**, aS-PL intensity when tuning the MIR photon energy (orange points) for MB (**a**) and RhB (**b**) molecules assembled in MSof cavities, compared to FTIR measurements in solution (grey). **c, d**, Power-dependent

integrated aS-PL intensity for increasing MIR (**c**) and pump (**d**) average powers, using MSof (orange) and NPof (yellow). Solid lines show power-law fits with an exponent of one. The detection noise floor is 100 cts s<sup>-1</sup>.

As the pump wavelength is tuned from 750 nm to 785 nm (Fig. 2e) while keeping the MIR wavelength at 6.16 μm (1,623 cm<sup>-1</sup>), the observed MIRVAL signal decreases. This is because the summed photon energy now drops below the  $|0\rangle \rightarrow |0'\rangle$  transition of MB. There is no change in the SERRS spectra on the Stokes side, confirming that MB dyes in the gap are not damaged. The spectrally integrated transduced signal versus pump wavelength follows the shape of the absorption curve of MB in solution (Fig. 2f), when rigidly shifted to lower energy by the MIR photon energy. This result is consistent for each MSof nanocavity measured, confirming that the observed aS-PL is the direct effect of MIR transduction. The signal is strong enough to now be seen at room temperature and for c.w. pumping. Intriguing changes in the aS-PL spectra arise for  $\lambda_{\text{pump}} > 765$  nm, corresponding to upconverted excitation below the  $|0\rangle \rightarrow |0'\rangle$  energy. These changes depend on the precise MIR and NIR plasmon resonance in each MSof (Supplementary Figs. 1–5 and Supplementary Section 1), thus implicating near-field plasmon enhancements. Exciting the vibrations by MIR light induces nuclear displacements set by the Huang–Rhys factors<sup>29</sup>, controlling the overall transfer of energy from  $|1_b\rangle$  to  $|0'\rangle$ . Here, the MIR-VAL intensity using MIR at 0.5 μW μm<sup>-2</sup> (our highest MIR power) is >10% of that when directly exciting  $|0\rangle \rightarrow |0'\rangle$  with a 633-nm pump of the same pump power as used in MIR-VAL. The observed aS-PL spectra have linewidths reduced by >30% compared with direct pumping (Supplementary Fig. 6). This suggests the suppression of inhomogeneous broadening, as a very small fraction of molecules participate in the MIR-VAL process, limited by the narrow MIR probe linewidth (0.1 cm<sup>-1</sup>).

To confirm that the MIR transduced signals originate from vibrations of the MB molecule, we tuned the MIR energy from 1,300 to 1,630 cm<sup>-1</sup> while keeping the pump fixed at 750 nm and using an individual MSof cavity (Fig. 3a). The percentage change in aS-PL intensity closely follows the vibrational absorption spectrum of MB molecules in solution obtained from conventional FTIR spectroscopy. The subtle differences are attributed to the effect of the plasmonic nanogap environment, compared to the normal ensemble solution spectra. The MIR transduced signal from  $\bar{n} = 40$  molecules has >10:1 signal-to-noise, with spectral resolution limited only by the linewidth of the quantum cascade laser (QCL) and step size used (4.2 cm<sup>-1</sup>). This has been

inaccessible in conventional FTIR measurements, even through surface-enhanced infrared absorption (SEIRA<sup>30</sup>) with single MSof cavities (Fig. 1e).

To demonstrate the generality of this aS-PL scheme, MSof systems were assembled in a similar manner but with rhodamine B (RhB) molecules in the gap (Supplementary Fig. 8). The MSof cavity was pumped with  $\lambda_{\text{pump}} = 633$  nm, below the  $|0\rangle \rightarrow |0'\rangle$  transition energy of RhB. An even larger aS-PL intensity change was now observed of >40% for 0.5 μW μm<sup>-2</sup>. MIR tuning experiments confirmed that the vibrational spectrum of RhB controls the transduction, and again is subtly different from ensemble measurements (Supplementary Fig. 9). In comparison to MB, which is scaffolded by the CB, the variation in the spectral signature of RhB originates from the different orientation of the molecules in the plasmonic gap. This changes both the electromagnetic and chemical selection rules. Different orientations of the RhB molecule experience different overlap of the exciton and vibrational dipole with the vertical electromagnetic fields in the nanogap. We modelled this with density-functional-theory calculations, showing changes in the intensity of vibrational peaks across different polarizations (Supplementary Fig. 10).

The current MIR detection limit was quantified through the observed power dependence (Fig. 3b,c). MIR transduced intensities are linear in both MIR and pump intensities, and linear with molecular concentration ( $\bar{n}$ ) in the gap (Supplementary Fig. 11). The MSof cavities provide tenfold better MIR-VAL efficiencies than the NPof cavities. This clearly demonstrates how MIR resonances enhance the coupling of MIR light to the vibrational transitions, matching the simulations (Supplementary Fig. 3). The system can be suitably modelled with rate equations of a four-level system (Supplementary Fig. 15 and Supplementary Section 2). Although the Purcell-enhanced aS-PL from  $|0'\rangle \rightarrow |0\rangle$  is incoherent (due to relaxation by intramolecular rotations and vibrations), the  $|0\rangle \rightarrow |0'\rangle$  transition is driven by the combination of MIR and pump light. The inherent quantum efficiency (QE) of the system of ~40% arises from its efficient radiative decay (Supplementary Fig. 3).

The heat absorption  $Q_a = I_{\text{MIR}}\sigma$ , with MIR intensity  $I_{\text{MIR}}$  and nanostructure absorption cross-section  $\sigma$ , with  $I_{\text{MIR}} = 2$  mW average power gave <1 °C heating, based on full simulations<sup>26</sup>. By contrast, the NIR



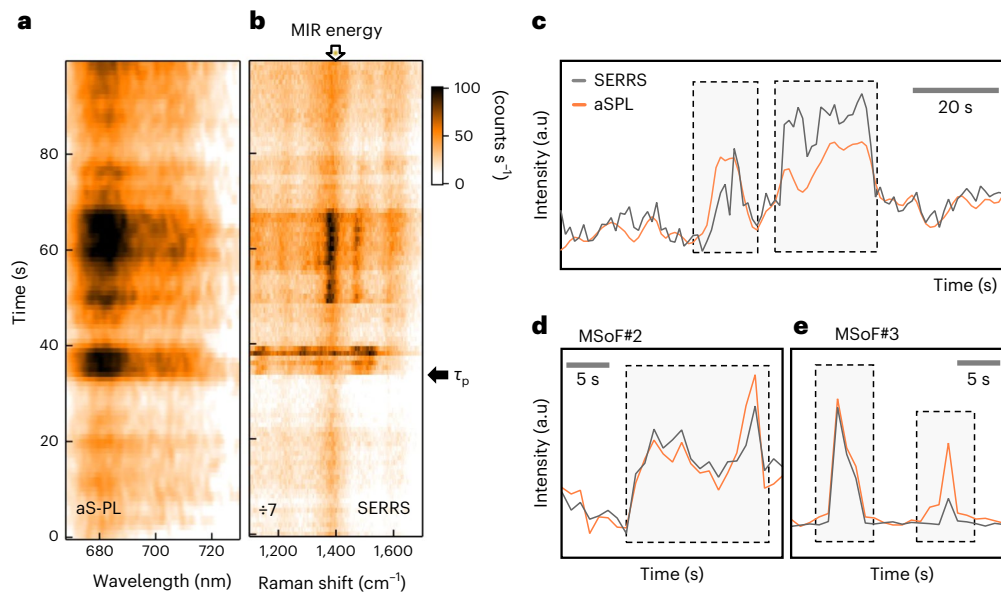


**Fig. 4 | MIR transduction of single molecules.** **a, b**, Repeated aS-PL and SERRS spectra for a single MSof cavity with a pump of  $0.5 \text{ mW } \mu\text{m}^{-2}$  at  $750 \text{ nm}$ . The top arrow shows MIR tuning. The transient picocavity event starts at  $\tau_p$ . **c**, Corresponding variations in the aS-PL and SERRS intensities exhibit strong

correlation. The picocavity regime is highlighted in black dashed boxes. **d, e**, Similar aS-PL and SERRS intensity tracks for another two different MSof cavities with pump of  $0.7 \text{ mW } \mu\text{m}^{-2}$  pump. Spectral maps are shown in Supplementary Fig. 12.

laser heating was  $>5 \text{ }^\circ\text{C}$  for  $200 \text{ } \mu\text{W}$  (ref. 31), yielding weak thermal upconversion, as seen in Fig. 2b, without MIR light. The exponential decay of anti-Stokes intensity fits a thermal distribution of electron-hole pairs in the metal given by  $I_{\text{as}} = A\{\exp(-\Delta E/(k_{\text{B}}T))\}^{-1}$ , where  $\Delta E$  is the energy difference of inelastically scattered light from the excitation frequency and  $k_{\text{B}}$  is the Boltzmann constant<sup>28</sup>. From these fits, the extracted temperature (Supplementary Fig. 7) from an average of  $>30$  scans is  $28 \pm 4 \text{ }^\circ\text{C}$ , and is unchanged when the MIR light is on. Furthermore, the  $443 \text{ cm}^{-1}$  SERRS vibration of MB does not vary in intensity when MIR is incident. This shows that thermal heating cannot account for the observed MIR-VAL signal.

From the noise floor of  $100 \text{ dark counts s}^{-1}$  (which drops substantially when spectrally integrating onto silicon detectors), we can easily measure average MIR powers of  $2.5 \text{ nW } \mu\text{m}^{-2}$  using a pump of  $80 \text{ } \mu\text{W } \mu\text{m}^{-2}$  for the MSof cavities. This corresponds to a noise-equivalent power (NEP) of  $31 \text{ nW Hz}^{-1/2}$ , which, accounting for the  $<0.1\%$  MIR coupling efficiency, implies an achievable NEP below  $30 \text{ pW Hz}^{-1/2}$  (Supplementary Section 3), better than available thermopiles and close to state-of-the-art mercury-cadmium-telluride cooled detectors. One source of noise is set by fluctuations in the ERS background emission due to the unstable gold nanostructure within the gap<sup>32</sup>, and can be suppressed by increasing the separation of  $\lambda_{\text{PL}}$  and  $\lambda_{\text{pump}}$ , and further by utilizing more stable plasmonic nanostructures<sup>33–35</sup>. Additional opportunities could involve exploring upconverted MIR from C–H bond vibrations at  $\lambda_{\text{MIR}} = 3.3 \text{ } \mu\text{m}$  or overtones of water in the range  $\lambda_{\text{MIR}} = 1–2 \text{ } \mu\text{m}$ .

The aS-PL transduction of MIR light has key advantages because of the fast rise time of detected photoluminescence. Using time-correlated single-photon lock-in methods<sup>36</sup>, the measured photoluminescence rise times are  $<100 \text{ ns}$  (Supplementary Fig. 11), currently limited by the QCL rise time. Theoretically, the aS-PL is Purcell-accelerated, and the high pump rates should give a response of  $<10 \text{ ps}$ , implying modulation speeds of  $>100 \text{ GHz}$ . Such high-frequency lock-in detection should further reduce the noise floor, stimulating requirements for developing matched low-cost, high-bandwidth MIR sources<sup>37</sup>.

As a final demonstration that this MIR detector can observe single molecules (Fig. 4), the pump was increased to  $0.5 \text{ mW } \mu\text{m}^{-2}$ . At this power, the light inside the nanocavity acts to transiently pull

single-metal-atom protrusions out of the facets. These generate a picocavity<sup>38</sup> where light is additionally confined around the adatom to volumes below  $1 \text{ nm}^3$ , and focused onto a single molecule. Such transient events are observed as new vibrational lines in SERRS (Fig. 4a,b, after  $\tau_p$ ), whose spectral fluctuations evidence their single-molecule origin<sup>38–43</sup>. Simultaneous recording of aS-PL and SERRS signals at  $t = 0 \text{ s}$  reveals weak upconversion with the MIR laser tuned to  $1,400 \text{ cm}^{-1}$  (Fig. 4b, arrow at the top). The presence of picocavities at  $t = 35 \text{ s}$  causes transient variations in aS-PL intensity that are precisely correlated in time with picocavity events in SERRS (Fig. 4c). This results in more than 200-fold enhancement of photoluminescence compared to dye molecules outside the picocavity in the nanocavity. This therefore provides the first experimental evidence for MIR absorption of a single vibrational bond (SEIRA).

We identified long-lived picocavities with RhB in MSof cavities, which allowed sweeping  $\lambda_{\text{MIR}}$  within their duration and extracting the vibrational spectra of single molecules within 1 min (Supplementary Fig. 13) using the MIR-VAL process. Multiple spectral scans collected within a single picocavity duration show the involvement of different vibrational modes in the dynamics. Such observations are only possible with picocavities, which support atomic-scale confinement around molecular bonds. It is possible to observe similar adatom effects with atomically sharp tips in scanning tunnelling microscopy (STM) geometries and break junctions, but their reproducibility, stability and scalability remain challenging. Here, adatom picocavities formed by light in self-assembled geometries overcome such issues, because the chemical and optical forces binding the adatoms to molecules are better understood<sup>44,45</sup>. Ongoing efforts to reconstruct vibrational spectra from full quantum simulations should thus recover adatom dynamics, metal-binding and the influence of ions and water at the nanoscale, which are long-term goals for progressing catalysis, electrochemistry, plasmonics and material science<sup>46,47</sup>.

MIR upconversion at the single-molecule level using picocavities can potentially access room-temperature broadband single-molecule infrared and Raman detection, capturing the full vibrational spectrum<sup>48–50</sup>. We show how to obtain single-molecule vibrational spectra spanning both infrared and Raman active modes, to study molecular motion. Measuring such single-molecule vibrational spectra is only

possible using the extreme confinement of picocavity optical fields. Simultaneous enhancements of Raman scattering, infrared absorption and fluorescence, which together enable MIRVAL, reveal the advantages of plasmonic confinement. Picocavities also provide an opportunity to highlight the interplay between electronic and vibrational states at the single-molecule level. The single-molecule method demonstrated here complements existing platforms in the visible<sup>41,42</sup>, and enables the discovery of rare molecular events, discontinuous kinetics and molecular subpopulations.

In summary, we have demonstrated optical readout of molecular vibrations down to the single-molecule level, and have shown applications in MIR detection and single-molecule vibrational absorption spectroscopy. The aS-PL signal observed from the absorption of MIR and NIR light in molecular bonds cannot be accounted for by thermal effects<sup>51</sup>, and provides clear advantages: infrared is absorbed in the ground state as opposed to a transient excited state<sup>52</sup>, and the emission is strongly Purcell-enhanced. Both applications demonstrated here rely on the MIR-VAL process, but the optimization of plasmonic cavity parameters is subtly different in each.

This technique resolves vibration-mediated upconversion of MIR to visible light through anti-Stokes photoluminescence. The large detector bandwidth (greater than gigahertz), room-temperature (or other) operation, straightforward large-scale fabrication and broad MIR tunability with potential for terahertz detection make this a highly promising scheme for real-world applications. Combining bottom-up and top-down nanoassembly gives manufacturable routes, but challenges include molecular degradation, metal instability and other noise sources. Using multiple MSoF cavities or nanoparticle aggregate multilayers<sup>53</sup>, an array detector can be created to enable MIR imaging down to the few-photon level. More generally, MSoF cavities that simultaneously trap MIR and visible light can enable few-molecule vibrational strong coupling to control chemistry<sup>54</sup> and act as a universal ‘chemiscope’<sup>55</sup> to observe chemical processes in plasmonic nanogaps. Future experiments will explore MIR multiplexing, the capability of using many types of dye molecule as well as solid-state emitters (such as PbS quantum dots, perovskites, nitrogen-vacancy centres or transition-metal dichalcogenides), alternative types of MIR, NIR resonators, different materials and light-emitting diode pumping. This demonstration enables molecular spectroscopy and sensing, as well as the quantum preparation of vibrational states for mode-selective chemistry and nano-optics.

## Online content

Any methods, additional references, Nature Portfolio reporting summaries, source data, extended data, supplementary information, acknowledgements, peer review information; details of author contributions and competing interests; and statements of data and code availability are available at <https://doi.org/10.1038/s41566-023-01263-4>.

## References

- Huang, K., Fang, J., Yan, M., Wu, E. & Zeng, H. Wide-field mid-infrared single-photon upconversion imaging. *Nat. Commun.* **13**, 1077 (2022).
- Dam, J. S., Tidemand-Lichtenberg, P. & Pedersen, C. Room-temperature mid-infrared single-photon spectral imaging. *Nat. Photon.* **6**, 788–793 (2012).
- Cheng, J.-X. & Xie, X. S. Vibrational spectroscopic imaging of living systems: an emerging platform for biology and medicine. *Science* **350**, 6264 (2015).
- Roellig, T. L. et al. Mid-infrared detector development for the Origins Space Telescope. *JATIS* **6**, 041503 (2020).
- Razeghi, M. & Nguyen, B.-M. Advances in mid-infrared detection and imaging: a key issues review. *Rep. Prog. Phys.* **77**, 082401 (2014).
- Rogalski, A. Infrared detectors: an overview. *Infrared Phys. Technol.* **43**, 187–210 (2002).
- Liu, C. et al. Silicon/2D-material photodetectors: from near-infrared to mid-infrared. *Light Sci. Appl.* **10**, 123 (2021).
- Staanum, P. F., Højbjerg, K., Skyt, P. S., Hansen, A. K. & Drewsen, M. Rotational laser cooling of vibrationally and translationally cold molecular ions. *Nat. Phys.* **6**, 271–274 (2010).
- Munsch, M. et al. Resonant driving of a single photon emitter embedded in a mechanical oscillator. *Nat. Commun.* **8**, 76 (2017).
- Yeo, I. et al. Strain-mediated coupling in a quantum dot–mechanical oscillator hybrid system. *Nat. Nanotechnol.* **9**, 106–110 (2014).
- Dorling, K. M. & Baker, M. J. Rapid FTIR chemical imaging: highlighting FPA detectors. *Trends Biotechnol.* **31**, 437–438 (2013).
- Taylor, A. B. & Zijlstra, P. Single-molecule plasmon sensing: current status and future prospects. *ACS Sens.* **2**, 1103–1122 (2017).
- Mao, X., Liu, C., Hesari, M., Zou, N. & Chen, P. Super-resolution imaging of non-fluorescent reactions via competition. *Nat. Chem.* **11**, 687–694 (2019).
- Griffiths, J. et al. Resolving sub-angstrom ambient motion through reconstruction from vibrational spectra. *Nat. Commun.* **12**, 6759 (2021).
- Kviatkovsky, I., Chrzanowski, H. M., Avery, E. G., Bartolomaeus, H. & Ramelow, S. Microscopy with undetected photons in the mid-infrared. *Sci. Adv.* **6**, eabd0264 (2010).
- Knez, D., Hanninen, A. M., Prince, R. C., Potma, E. O. & Fishman, D. A. Infrared chemical imaging through non-degenerate two-photon absorption in silicon-based cameras. *Light Sci. Appl.* **9**, 125 (2020).
- Chen, W. et al. Continuous-wave frequency upconversion with a molecular optomechanical nanocavity. *Science* **374**, 1264–1267 (2021).
- Xomalis, A. et al. Detecting mid-infrared light by molecular frequency upconversion in dual-wavelength nanoantennas. *Science* **374**, 1268–1271 (2021).
- Gilani, A. G., Salmanpour, M. & Ghorbanpour, T. Solvatochromism, dichroism and excited state dipole moment of azure A and methylene blue. *J. Mol. Liq.* **179**, 118–123 (2013).
- Kasha, M. Characterization of electronic transitions in complex molecules. *Discuss. Faraday Soc.* **9**, 14–19 (1950).
- Mamin, H. J. et al. Nanoscale nuclear magnetic resonance with a nitrogen-vacancy spin sensor. *Science* **339**, 557–560 (2013).
- Staudacher, T. et al. Nuclear magnetic resonance spectroscopy on a (5-nanometer)<sup>3</sup> sample volume. *Science* **339**, 561–563 (2013).
- Laubereau, A., Seilmeier, A. & Kaiser, W. A new technique to measure ultrashort vibrational relaxation times in liquid systems. *Chem. Phys. Lett.* **36**, 232–237 (1975).
- Whaley-Mayda, L., Guha, A., Penwell, S. B. & Tokmakoff, A. Fluorescence-encoded infrared vibrational spectroscopy with single-molecule sensitivity. *J. Am. Chem. Soc.* **143**, 3060–3064 (2021).
- Chikkaraddy, R. & Baumberg, J. J. Accessing plasmonic hotspots using nanoparticle-on-foil constructs. *ACS Photonics* **8**, 2811–2817 (2021).
- Chikkaraddy, R., Xomalis, A., Jakob, L. A. & Baumberg, J. J. Mid-infrared-perturbed molecular vibrational signatures in plasmonic nanocavities. *Light Sci. Appl.* **11**, 19 (2022).
- Chikkaraddy, R. et al. Single-molecule strong coupling at room temperature in plasmonic nanocavities. *Nature* **535**, 127–130 (2016).
- Mertens, J., Kleemann, M.-E., Chikkaraddy, R., Narang, P. & Baumberg, J. J. How light is emitted by plasmonic metals. *Nano Lett.* **17**, 2568–2574 (2017).

29. von Cosel, J. et al. Vibrationally resolved electronic spectra including vibrational pre-excitation: theory and application to VIPER spectroscopy. *J. Chem. Phys.* **147**, 164116 (2017).
30. Neubrech, F., Huck, C., Weber, K., Pucci, A. & Giessen, H. Surface-enhanced infrared spectroscopy using resonant nanoantennas. *Chem. Rev.* **117**, 5110–5145 (2017).
31. Xomalis, A. et al. Controlling optically driven atomic migration using crystal-facet control in plasmonic nanocavities. *ACS Nano* **14**, 10562–10568 (2020).
32. Carnegie, C. et al. Flickering nanometre-scale disorder in a crystal lattice tracked by plasmonic flare light emission. *Nat. Commun.* **11**, 682 (2020).
33. Chaudhuri, K. et al. Remote sensing of high temperatures with refractory, direct-contact optical metacavity. *ACS Photonics* **7**, 472–479 (2020).
34. Li, W. et al. Refractory plasmonics with titanium nitride: broadband metamaterial absorber. *Adv. Mater.* **26**, 7959–7965 (2014).
35. Chikkaraddy, R. et al. Boosting optical nanocavity coupling by retardation matching to dark modes. *ACS Photonics* **10**, 493–499 (2023).
36. Jakob, L. A. et al. Single photon multiclock lock-in detection by picosecond timestamping. *Optica* **8**, 1646–1653 (2021).
37. Popa, D. et al. A highly stable, nanotube-enhanced, CMOS-MEMS thermal emitter for mid-IR gas sensing. *Sci. Rep.* **11**, 22915 (2021).
38. Benz, F. et al. Single-molecule optomechanics in ‘picocavities’. *Science* **354**, 726–729 (2016).
39. Maher, R. C. et al. Physics of single molecule fluctuations in surface enhanced Raman spectroscopy active liquids. *J. Chem. Phys.* **121**, 8901–8910 (2004).
40. Sonntag, M. D., Chulhai, D., Seideman, T., Jensen, L. & Van Duyne, R. P. The origin of relative intensity fluctuations in single-molecule tip-enhanced Raman spectroscopy. *J. Am. Chem. Soc.* **135**, 17187–17192 (2013).
41. Kulzer, F. & Orrit, M. Single-molecule optics. *Annu. Rev. Phys. Chem.* **55**, 585–611 (2004).
42. Xie, X. S. & Trautman, J. K. Optical studies of single molecules at room temperature. *Annu. Rev. Phys. Chem.* **49**, 441–480 (1998).
43. Orrit, M., Ha, T. & Sandoghdar, V. Single-molecule optical spectroscopy. *Chem. Soc. Rev.* **43**, 973–976 (2014).
44. Baumberg, J. J. Picocavities: a primer. *Nano Lett.* **22**, 5859–5865 (2022).
45. Häkkinen, H. The gold–sulfur interface at the nanoscale. *Nat. Chem.* **4**, 443–455 (2012).
46. Mitchell, S. & Pérez-Ramírez, J. Single atom catalysis: a decade of stunning progress and the promise for a bright future. *Nat. Commun.* **11**, 4302 (2020).
47. Wu, T., Yan, W. & Lalanne, P. Bright plasmons with cubic nanometer mode volumes through mode hybridization. *ACS Photonics* **8**, 307–314 (2021).
48. Zirkelbach, J. et al. High-resolution vibronic spectroscopy of a single molecule embedded in a crystal. *J. Chem. Phys.* **156**, 104301 (2022).
49. Arroyo, J. O. & Kukura, P. Non-fluorescent schemes for single-molecule detection, imaging and spectroscopy. *Nat. Photon.* **10**, 11–17 (2016).
50. Xiong, H. et al. Stimulated Raman excited fluorescence spectroscopy and imaging. *Nat. Photon.* **13**, 412–417 (2019).
51. Roman, B. J. & Sheldon, M. T. Six-fold plasmonic enhancement of thermal scavenging via CsPbBr<sub>3</sub> anti-Stokes photoluminescence. *Nanophotonics* **8**, 599–605 (2019).
52. Liang, L., Wang, C., Chen, J., Wang, Q. J. & Liu, X. Incoherent broadband mid-infrared detection with lanthanide nanotransducers. *Nat. Photon.* **16**, 712–717 (2022).
53. Arul, R. et al. Giant mid-IR resonant coupling to molecular vibrations in sub-nm gaps of plasmonic multilayer metafilms. *Light Sci. Appl.* **11**, 281 (2022).
54. Garcia-Vidal, F. J., Ciuti, C. & Ebbesen, T. W. Manipulating matter by strong coupling to vacuum fields. *Science* **373**, eabd0336 (2021).
55. Petek, H. Single-molecule femtochemistry: molecular imaging at the space-time limit. *ACS Nano* **8**, 5–13 (2014).

**Publisher's note** Springer Nature remains neutral with regard to jurisdictional claims in published maps and institutional affiliations.

**Open Access** This article is licensed under a Creative Commons Attribution 4.0 International License, which permits use, sharing, adaptation, distribution and reproduction in any medium or format, as long as you give appropriate credit to the original author(s) and the source, provide a link to the Creative Commons license, and indicate if changes were made. The images or other third party material in this article are included in the article's Creative Commons license, unless indicated otherwise in a credit line to the material. If material is not included in the article's Creative Commons license and your intended use is not permitted by statutory regulation or exceeds the permitted use, you will need to obtain permission directly from the copyright holder. To view a copy of this license, visit <http://creativecommons.org/licenses/by/4.0/>.

© The Author(s), 2023

## Methods

### Sample preparation

To prepare the thin mirror, we deposited 10 nm of Au onto clean Si membranes of 200- $\mu\text{m}$  thickness with a deposition rate of  $0.5 \text{ \AA s}^{-1}$  (Moorfield nanoPVD-T15A thermal evaporator). The Au-coated substrates were dipped into 0.1 mM MB-CB solution for 12 h, resulting in a self-assembled monolayer of MB-CB on the gold. For the Ag MSoF optical cavities, 4- $\mu\text{m}$ -diameter Ag-coated microspheres (Cospheric, Ag thickness of 50 nm) dispersed in ethanol were deposited directly onto the MB-CB assembled Au-coated Si substrates. The deposition time was kept below 90 s, resulting in well-dispersed AgMSs. Finally, the samples were rinsed thoroughly with ethanol to remove any unbound AgMSs.

### Infrared microscopy

FTIR reflection spectra on individual MSoF cavities were recorded using a Shimadzu AIM-9000 FTIR microscope, equipped with a liquid-nitrogen-cooled MCT detector and Cassegrain  $\times 15$  objective with numerical aperture (NA) of 0.5. The spectra were referenced to a clean Au mirror.

### Experimental set-up

The details of the optical set-up are available in ref. 26. All SERS and aS-PL spectroscopy measurements were performed in a custom-built dual-channel microscope. A tunable c.w. Ti:sapphire laser was used as the pump, which was spectrally filtered using an angle-tuned 785-nm cleanup filter. The laser was focused into the sample with a 0.9-NA objective lens with  $150 \mu\text{W } \mu\text{m}^{-2}$  average power on the sample (where not otherwise noted). The back-scattered light was collected from the sample objective and filtered with two angle-tuned notch filters before routing it to a Shamrock i303 spectrograph and a Newton electron multiplying charge coupled device (Andor). For imaging, the reflected light collected through the same objective lens was directed to a camera (Lumenera Infinity 3-1).

For the MIR light source, a LaserTune IR source (Block) with a wavelength range of 5.4–13  $\mu\text{m}$  was used with a maximum average output of  $500 \mu\text{W}$  ( $\sim 2 \times 4\text{-mm}$  beam, collimated) with  $<5\%$  duty cycle. The pump (MIR light) was co-aligned with the probe (visible light) using a 0.5-NA Cassegrain objective lens. The modulation of the pump laser was synced with the QCL using an acousto-optic modulator and function generator. The sample was placed on a fully automated motorized stage (Prior Scientific HI01) controlled with code written in Python.

For single-photon time-correlated measurements, the arrival times of all photons at the detector (Micro Photon Devices PDM PD-100-CTD) and reference signals (MIR laser trigger) were continuously recorded by time-to-digital converters on a field-programmable gate array board. Comparing the photon timestamps with the reference signal allowed recreation of the periodic perturbation of the SERS

signal by the MIR laser in time, integrated over millions of modulation cycles. This single-photon lock-in detection scheme is described in more detail elsewhere<sup>36</sup>.

### Data availability

The data that support the findings of this study are available from the corresponding author upon reasonable request and data for all figures can be found at <https://doi.org/10.17863/CAM.100099>.

### Acknowledgements

This work was supported by the European Research Council (ERC) under Horizon 2020 research and innovation programme PICOFORCE (grant no. 883703), THOR (grant no. 829067), POSEIDON (grant no. 861950) and the Engineering and Physical Sciences Research Council (EPSRC; EP/L015978/1, EP/L027151/1, EP/S022953/1, EP/P029426/1 and EP/R020965/1) (to J.J.B.). Further funding was provided by the Royal Society (RGS\R1\231458) to R.C. R.C. also acknowledges support from Trinity College, University of Cambridge. R.A. acknowledges support from the Rutherford Foundation of the Royal Society Te Apārangi of New Zealand, and the Winton Programme for the Physics of Sustainability.

### Author contributions

R.C. and J.J.B. conceived and designed the experiments. R.C. performed the experiments with input from R.A. and L.A.J. R.A. carried out the FTIR and RhB measurements. R.C. performed the simulation and the analytical modelling. R.A. performed the DFT simulations. R.C., R.A. and J.J.B. analysed the data. R.C., R.A. and J.J.B. wrote the paper with input from all authors.

### Competing interests

The authors declare no competing interests, but have filed IP on this technology (patent application no. UK 2203507.5).

### Additional information

**Supplementary information** The online version contains supplementary material available at <https://doi.org/10.1038/s41566-023-01263-4>.

**Correspondence and requests for materials** should be addressed to Rohit Chikkaraddy or Jeremy J. Baumberg.

**Peer review information** *Nature Photonics* thanks Matthew Sheldon and the other, anonymous, reviewer(s) for their contribution to the peer review of this work.

**Reprints and permissions information** is available at [www.nature.com/reprints](http://www.nature.com/reprints).